inorganics

MDPI

Article

Microstructure and Electrochemical Properties of Pure and Vanadium-Doped $Li_4Ti_5O_{12}$ Nanoflakes for High Performance Supercapacitors

Mudda Deepak [1], Obili M. Hussain [1,*] and Christian M. Julien [2,*]

[1] Thin Films Laboratory, Physics Department, Sri Venkateswara University, Tirupati 517502, India; deepakmudda7@gmail.com
[2] Institut de Minéralogie, de Physique des Matériaux et Cosmologie (IMPMC), Sorbonne Université, UMR-CNRS 7590, 4 Place Jussieu, 75252 Paris, France
* Correspondence: hussainsvu@gmail.com (O.M.H.); christianjulien716@gmail.com (C.M.J.)

Abstract

Nanostructured binary metal oxides have demonstrated the potential for increased electrochemical performance due to their structural stability, electronic conductivity, and various oxidation states. The $Li_4Ti_5O_{12}$ was successfully synthesized via a hydrothermal procedure at different reaction periods (12, 18, and 24 h), and its microstructural and supercapacitive characteristics were studied. The XRD and XPS studies confirm the formation of $Li_4Ti_5O_{12}$ in pure phase when synthesized at 24 h (LTO@24) of reaction time. FESEM and HRTEM images reveal nanoflake surface morphology. Both LTO@24 and V-LTO@24 nanoflakes exhibited impressive electrochemical performance, with specific capacitance values of 357 and 442 F $g^{-1,}$ respectively, at 1 A g^{-1}. The V-LTO@24 showed remarkable supercapacitor properties, demonstrating excellent rate capability and cycleability that surpass those of pure LTO@24.

Keywords: $Li_4Ti_5O_{12}$ nanoflakes; hydrothermal synthesis; microstructure; vanadium doping; electrochemical properties; supercapacitors

check for updates

Academic Editors: Zhoupeng Li, Zixuan Liu and Deyu Wang

Received: 22 May 2025
Revised: 28 June 2025
Accepted: 29 June 2025
Published: 1 July 2025

Citation: Deepak, M.; Hussain, O.M.; Julien, C.M. Microstructure and Electrochemical Properties of Pure and Vanadium-Doped $Li_4Ti_5O_{12}$ Nanoflakes for High Performance Supercapacitors. *Inorganics* **2025**, *13*, 223. https://doi.org/10.3390/inorganics13070223

Copyright: © 2025 by the authors. Licensee MDPI, Basel, Switzerland. This article is an open access article distributed under the terms and conditions of the Creative Commons Attribution (CC BY) license (https://creativecommons.org/licenses/by/4.0/).

1. Introduction

The fast-increasing energy crunch and depletion of fossil fuel resources have prompted researchers to investigate efficient energy storage systems such as batteries and supercapacitors. Batteries are the most utilized energy devices owing to their high energy capacity, whereas capacitors remain the preferred choice even to date when considerable energy is required at high power. In recent times, supercapacitors have been observed as a fabulous consideration owing to their high energy density, excellent reversibility, rapid charge/discharge capability, and extended cycle life [1–4]. However, they have been encountering performance degradation and diminutive cycle stability for long-term current solutions [5,6]. The development of flexible, lightweight, environmentally friendly, and efficient energy storage devices with high energy and power densities mainly depends on the fabrication of suitable electrode material with required properties and is one of the key issues of current research [7–9].

Transition-metal oxides (TMOs) have been extensively considered as electrode materials due to their superior physicochemical properties, such as multiple valences, fast ion/electron transport, and good structural stability as electrodes in high-efficiency lithium-ion batteries

(LIBs) and supercapacitors (SCs). Though these TMOs elude the formation of Li dendrites, numerous challenges such as poor intrinsic electrical conductivity, significant volume alteration during intercalation, voltage lapses between charge–discharge and electrode decomposition are yet to be addressed [10–12]. Many transition-metal oxides (TMOs), such as MnO_2, Co_3O_4, MoO_3, $LiCoO_2$, $LiMn_2O_4$, $NiCoO_2$, $MnCoO_2$, $Mn(OH)_2$, $Ni(OH)_2$, Li_2TiO_3, etc., have been commercially employed in LIBs and supercapacitors [13–21]. Among TMOs, lithium titanate (LTO) epitomizes the solid solution $Li_{3+x}Ti_{6-x}O_{12}$ ($0 \leq x \leq 1$) family with a crystal structure that belongs to the $Fd\bar{3}m$ space group. Part of Li^+ are located at 8*a* Wyckoff sites and all Ti-ions and another part of Li^+ are positioned at 16*d* sites at a ratio of Li:Ti = 1:5, whereas oxygen-ions inhabit the 32*e* sites and hence LTO can be chemically designated as $Li_{3(8a)}[LiTi_5^{4+}]_{(16d)}O_{12(32e)}$. The spinel lithium titanate (LTO) is a potential anode material that can replace graphite because it provides a high voltage of 1.55 V against Li insertion, high power density (~10 kW kg^{-1}), and outstanding structural stability with zero strain during intercalation. In addition, excellent pseudo-capacitive behavior, a Faradaic process, has been identified in some modified LTO to transcend the limit of theoretical capacity by improving the lithium-ion storage, providing high power and energy densities over a varied temperature range. However, the poor electronic conductivity due to a dearth of electrons in the 3*d* orbital of Ti and the low Li diffusion coefficient impede the electrochemical performance of LTO for practical use in LIBs and SCs [22–25]. The pseudocapacitive behavior of LTO may be significantly enriched by employing synergistic effects of multiple modifications by creating additional active sites. Intensive investigations have been made over the past one decade to improve reversible specific capacity and superior rate capability by adopting several strategies such as morphological engineering by optimizing the size and shape of nanoparticles, doping with a suitable metallic or non-metallic ions, formation of nano composite with carbonaceous materials (CNTs/rGO), heterogeneous phase control, etc. Several researchers synthesized LTO in various compositions and nano-structural designs utilizing various fabrication techniques to enhance the electrochemical performance for utilization in high-efficiency energy storage devices. Further, attempts were also made to improve the electrical conductivity of $Li_4Ti_5O_{12}$ by doping with a suitable transition metal cation into Li or Ti sites [26,27].

Among the potential dopants, vanadium is distinguished as a noteworthy contender owing to its superior electrical conductivity and redox properties. Vanadium oxides have been extensively researched as electrochemical energy storage materials for supercapacitors and lithium-ion batteries due to their capacity for redox intercalation, attributed to the diverse oxidation states of vanadium (+2, +3, +4, and +5). V is an exceptionally suitable dopant for LTO, as it maintains the integrity of its phase and lattice parameters because of the compatibility between the ionic radii of Ti^{4+} and V^{5+} [8]. Multiple reports discussed the utility of LTO and vanadium-doped LTO in the context of Li-ion batteries and hybrid supercapacitors [28,29]. A detailed review on advanced pseudocapacitive lithium titanate towards next-generation energy storage devices was reported by Ge et al. [23]. Several researchers reported the synthesis of LTO in typical surface morphologies, including nanoparticles, nanowires, and nanosheets, and demonstrated notable pseudocapacitive contributions. Batsukh et al. [30] synthesized LTO materials via the solid-state method and reported a maximum specific capacitance of 3.59 F g^{-1}. Tian et al [31] synthesized LTO consisting of ultrafine nanowires by ion exchange process in a liquid phase environment and demonstrated a specific capacity of ~178 mAh g^{-1} at 200 mA g^{-1} even after 2500 cycles. Xing et al [26] synthesized $Li_4Ti_5O_{12}$–graphene hybrid micro/nanostructures and pine needles by an effective hydrothermal process and demonstrated specific capacitances of 706 F g^{-1} and 314 F g^{-1} at 1 A g^{-1}, respectively, with cycle retention of 90%. Lee et al [32] fabricated asymmetric hybrid supercapacitors using $Li_4Ti_5O_{12}$ as an electrode and reported a high specific capacitance of 63 F g^{-1}.

The current research work involves the synthesis of $Li_4Ti_5O_{12}$ nanoflakes by the hydrothermal technique at various reaction times and optimized with respect to the microstructural properties. The synthesized $Li_4Ti_5O_{12}$ nanoflakes at a reaction period of 24 h demonstrated exceptional electrochemical performance with a specific capacitance of 357 F g^{-1} at a current density of 1 A g^{-1}. For further enhancement of electrical conductivity and hence the specific capacitance, the $Li_4Ti_5O_{12}$ is doped with vanadium and reported 442 F g^{-1} at 1 A g^{-1} current density with admirable rate capability and cycle stability.

2. Results and Discussion

2.1. Studies of Pristine $Li_4Ti_5O_{12}$ Nanoflakes

2.1.1. XRD Analysis

The XRD analysis was employed to confirm the crystalline structure and phase purity of the hydrothermally synthesized $Li_4Ti_5O_{12}$ Nanoflakes. Figure 1 illustrates the XRD spectra of $Li_4Ti_5O_{12}$ nanopowders synthesized at various reaction time periods. The XRD spectra of $Li_4Ti_5O_{12}$ synthesized for 12 and 18 h displayed an additional minor anatase (A) and rutile (R) phase of TiO_2 at $2\theta = 25.30°$ (JCPDS card 21-1272) and $2\theta = 27.47°$ (JCPDS card 12-1276), respectively, alongside the $Li_4Ti_5O_{12}$ phase. This phenomenon may be attributed to inadequate reaction times, leading to incomplete phase transformation and the presence of residual TiO_2 [33,34]. By extending the reaction time to 24 h, the XRD reflections associated with the TiO_2 phases are no longer present, while peaks corresponding to the cubic spinel $Li_4Ti_5O_{12}$ phase emerged. The spectrum showed predominantly (111) orientation at a 2θ value of 18.30° along with the other diffraction peaks corresponding to the planes of the cubic spinel $Li_4Ti_5O_{12}$ structure with the $Fd\bar{3}m$ space group (JCPDS card 49-0207) [35–37]. The results indicate that the product progressively converted to the pure cubic spinel $Li_4Ti_5O_{12}$ by the extension of reaction time to 24 h.

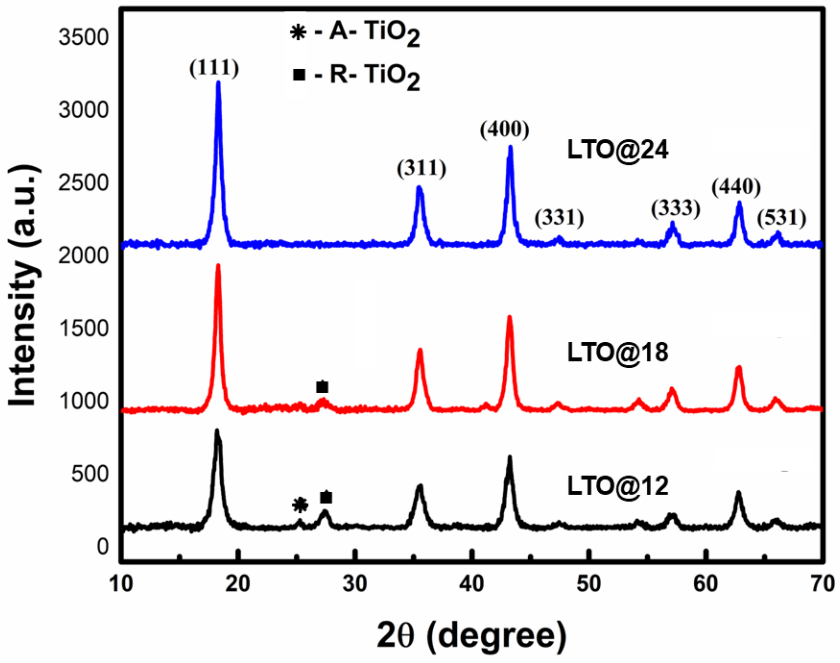


Figure 1. XRD pattern of $Li_4Ti_5O_{12}$ nanoflakes synthesized hydrothermally at various time periods. Marks ■ and ✱ indicate the presence of the A-TiO_2 and R-TiO_2 phases, respectively.

The Debye–Scherrer formula was used to estimate the crystallite size (L) of the as-produced samples using all XRD reflections:

$$L = \frac{k\lambda}{\beta cos\theta}, \quad (1)$$

where θ is the Bragg angle, β is the full width at half-maximum, λ is the wavelength of X-ray radiation, and k is equal to 0.9. Additionally, dislocation density (δ), microstrain (ε), and unit volume (V) values are calculated (see Table 1) based on the following relations [35,38]:

$$\delta = \frac{1}{L^2}, \quad (2)$$

$$\varepsilon = \frac{\beta\ cos\theta}{4}, \quad (3)$$

$$V = a^3, \quad (4)$$

$$d = \frac{a}{\sqrt{h^2 + k^2 + l^2}}, \quad (5)$$

Table 1. The crystallographic parameters of LTO nano powder samples synthesized under various conditions.

Sample	Crystallite Size (nm)	Dislocation Density (δ)	Microstrain (rd)	Lattice Parameter (Å)	Unit Volume (Å^3)
LTO@12	11	8.27652×10^{15}	0.009933	8.4117(0)	595.18
LTO@18	12	6.98751×10^{15}	0.008899	8.4018(2)	593.08
LTO@24	13	6.31196×10^{15}	0.00827	8.3671(8)	585.76
V-LTO@24	11.8	7.7152×10^{15}	0.0088	8.3401(2)	580.11

The results in Table 1 show that the size of the crystallites increases as the hydrothermal reaction time increases from 12 to 24 h. The unit cell volume of LTO synthesized at 24 h and the estimated lattice parameter value a deduced from Equations (4) and (5) are in good agreement with the reported value [39–41]. Nanoparticles of smaller crystallites have a higher surface area-to-volume ratio, which is important for strengthening the electrode/electrolyte interface, facilitating quicker ion diffusion, and increasing the material's charge storage capacity.

2.1.2. Surface Morphology Analysis

The surface morphological features of the material are an essential aspect that is intricately linked to the specific surface area, diffusion pathways, surface-to-volume ratios, and consequently, the performance of supercapacitors. The surface microstructure of hydrothermal-synthesized $Li_4Ti_5O_{12}$ nanoparticles is characterized using FE-SEM. Figure 2 presents the SEM micrographs of $Li_4Ti_5O_{12}$ nanoparticles at various magnifications, prepared through the hydrothermal method at different reaction times. The influence of reaction time on surface morphology is distinctly evident in the SEM micrograph. Figure 2a,b show the SEM images of the $Li_4Ti_5O_{12}$ sample synthesized at 12 h. The SEM images demonstrate the formation of interconnected nanoflakes forming three-dimensional flower-like structures. In high magnification SEM images, the assembly of nanoparticles with nanoflake-like structures having a rough surface, non-uniform size, and thinner nanoflakes with uneven edges may be due to the short hydrothermal reaction times. The surface morphology was seen to alter when reaction time

varied from 12 to 18 h. The formation of nanoflakes of varied sizes with well-defined edges is observed at a reaction time of 18 h, as seen in Figure 2c,d. Furthermore, prolonging the reaction period to 24 h resulted in the formation of a well-defined, smooth surface with assembly of relatively uniform length of the nanoflakes, which were about 60 nm long and 20 nm wide, as shown in Figure 2e,f. Because of the prolonged reaction time, the flakes became firmly packed together and eventually formed a micro-network. These results indicate that the reaction time plays a pivotal on the surface morphology of nanostructures. The dimensional nanoflakes have a porous nature and a good surface area. This type of structure significantly minimizes the resistance associated with electrolyte penetration and diffusion, while facilitating rapid ion and electron transfer. Additionally, it offers an ample effective area for interactions between electrolyte ions and active materials, enhancing Faradaic reactions during the electrochemical process [42–45].

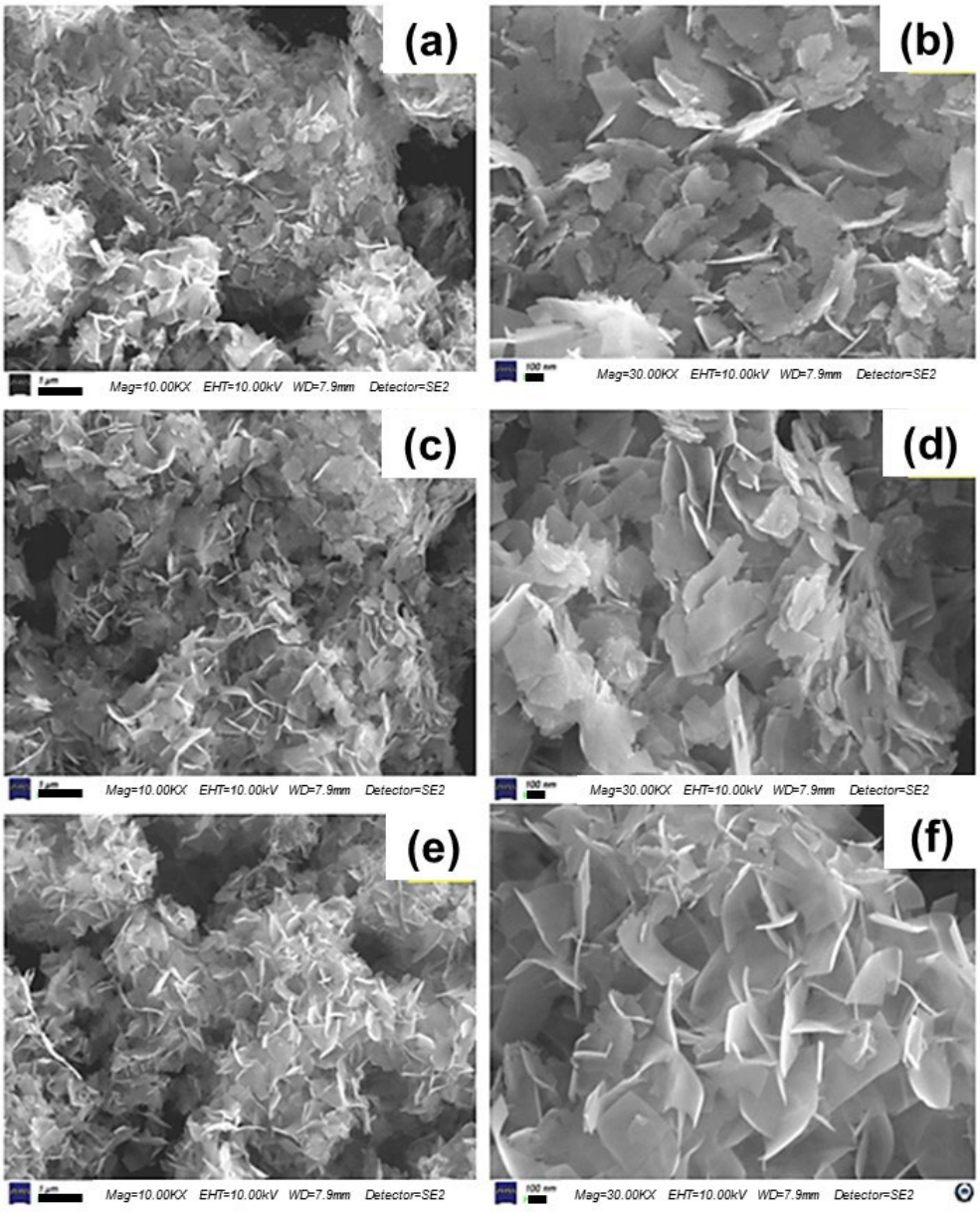


Figure 2. FESEM images of $Li_4Ti_5O_{12}$ synthesized at different reaction time periods: (**a**,**b**) 12 h, (**c**,**d**) 18 h, and (**e**,**f**) 24 h ((**a**,**c**,**e**) low magnification scale μm, (**b**,**d**,**f**) high magnification, scale 100 nm).

HRTEM is used as a representative to further characterize the shape and structure of the $Li_4Ti_5O_{12}$ nanoflakes. Figure 3 displays the typical TEM micrographs for the 24 h

sample. The TEM image in Figure 3a demonstrates structural characteristics of $Li_4Ti_5O_{12}$ nanoflakes, which are consistent with the observations of the SEM data. The Fourier transformation (FFT) derived from the HRTEM image of nanoflakes distinctly reveals a symmetrical pattern, as exemplified in the inset of Figure 3b. The measured interplanar distance (d-spacing) of 0.48 nm corresponds to the (111) crystallographic plane of the $Li_4Ti_5O_{12}$ spinel structure. Figure 3c shows the selected area electron diffraction pattern with the indexed diffraction planes of (111), (222), (331), and (531) corresponding to the cubic spinel $Li_4Ti_5O_{12}$ structured phase, indicating the polycrystalline nature of $Li_4Ti_5O_{12}$. HRTEM pictures shown in Figure 3b,c confirm the phase purity of the produced $Li_4Ti_5O_{12}$ Nanoflakes.

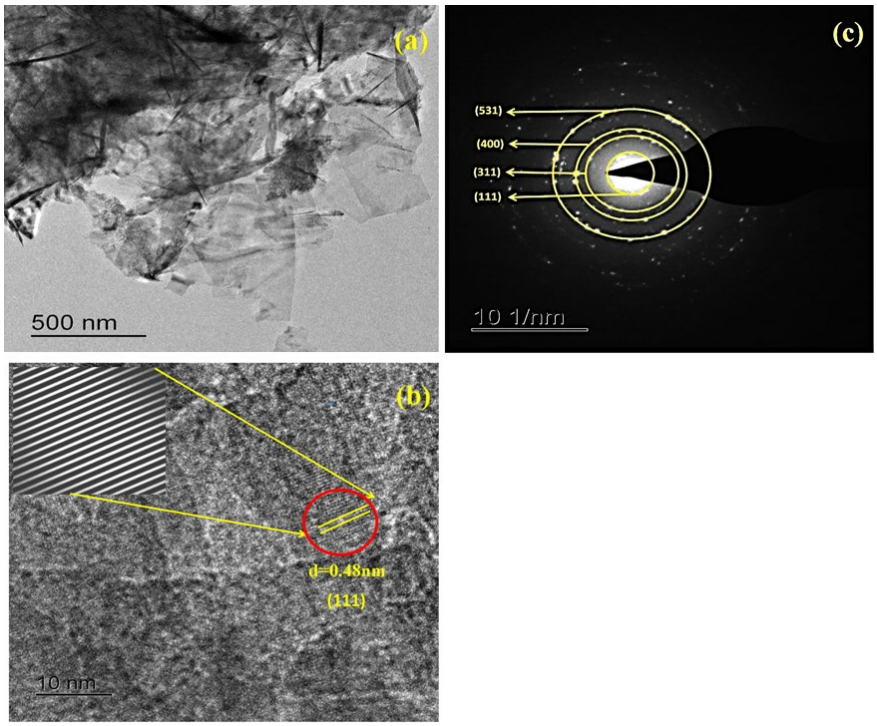


Figure 3. Microstructural features of LTO@24: (**a**) TEM image, (**b**) HRTEM image showing the lattice fringe width of 0.48 nm, and (**c**) SAED pattern.

2.1.3. XPS Analysis

The XPS measurements were piloted to analyze the chemical composition and metal oxidation states of $Li_4Ti_5O_{12}$@24 nanoflakes, as shown in Figure 4. The presence of Li, Ti, and O elements is confirmed by the XPS survey spectrum presented in Figure 4a. The Li 1s core level XPS spectrum shown in Figure 4b in the low binding energy region displays a Li 1s peak at 54.8 eV, which is attributed to the Li-O bond. The Ti 2p core level XPS spectrum, as illustrated in Figure 4c, displays a distinct set of Ti $2p_{1/2}$ and $2p_{3/2}$ lines doublet peaks at about 464.7 and 459 eV, respectively, which are indicative of the Ti^{4+} state. The O 1s peak at about 530.4 eV corresponds to metal–oxygen bonds and is shown in Figure 4d. The presence of core-level binding energy peaks is almost similar to the reported values and confirms the phase purity and chemical purity of the LTO spinel phase [26].

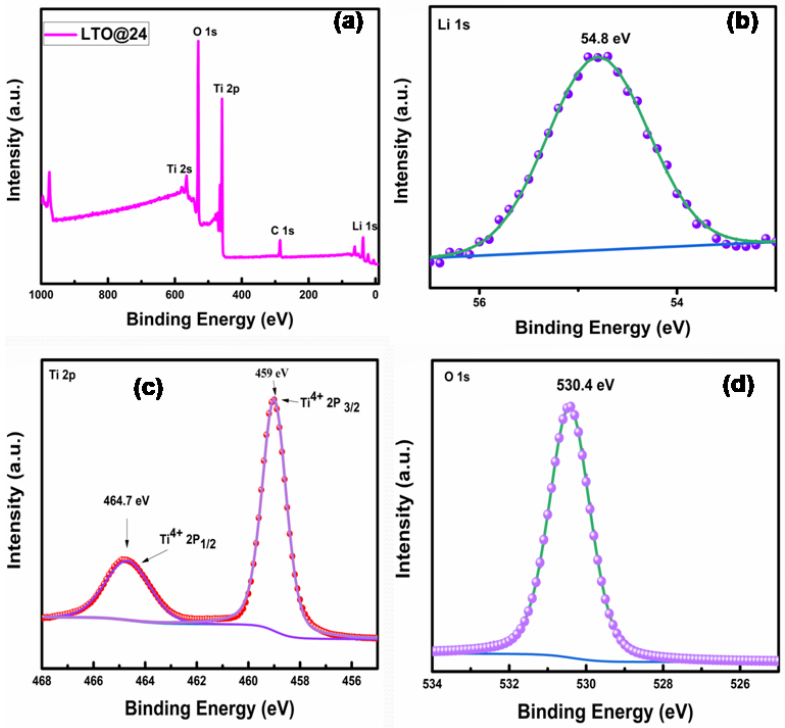


Figure 4. (**a**) X-ray photoelectron spectra of LTO@24, (**b**–**d**) high-resolution XPS survey spectra of Li 1s, Ti 2p, and O 1s, respectively.

2.1.4. Electrochemical Analysis

The electrochemical properties of $Li_4Ti_5O_{12}$ nanoflakes synthesized by a hydrothermal method were carried out by a three-electrode system in 1 mol L^{-1} KOH aqueous electrolyte, and the data is shown in Figure 5. The C measurements were conducted at different scan rates from 1 to 50 mV s^{-1} in the potential range of −0.3–0.6 V vs. Ag/AgCl. The CV plots of LTO electrodes exhibited a couple of well-defined oxidation/reduction peaks attributed to the reversible faradic reactions. The marginal shift towards a lower potential of the cathodic peak and shift of the anodic peak towards a higher potential with scan rate has been observed from CV plots (Figure 5a). The polarization value, which is the difference between the cathodic and anodic peaks, is observed to be decreased with the increasing scan rate, representing the fast kinetics and reversibility in the electrode, and the redox process is governed by Ti^{+3}/Ti^{+4}. The increased voltametric currents in association with the marginal shift in the peak potential by increasing the scan rate indicate outstanding rate performance and electrochemical reversibility. The flake-like morphology of the LTO@24 electrode supports fast electron/ion transfer between the electrode and electrolyte, and hence, increases the total amount of charge storage due to the contributions of both capacitive and intercalation/deintercalation mechanisms. Additionally, the total charge accumulated in the LTO electrode as a result of the redox reaction was determined using the area under the current-voltage curve at a constant scan rate. The specific capacitance C_s of the electrode at each scan rate was calculated using the subsequent Equation (6) [46]:

$$C_s = \frac{1}{m\nu\Delta V}\int_{V_a}^{V_c} I(V)dV, \quad (6)$$

where ν is the potential scanning rate, m denotes the mass of active electrode material, and $\Delta V = V_c - V_a$ represents the potential window for the discharging process. The estimated specific capacity values of LTO@12 and LTO@18 form CV plots (CV plots are provided in Figures S1 and S2 (Supplementary Materials file)) are 50 and 91 F g^{-1}, respectively,

at 1 mV s^{-1}. The lower value of specific capacities is because of the presence of additional phases and the formation of small nanoflakes with different sizes and uneven edges due to short hydrothermal reaction time periods. The specific capacities of the LTO@24 electrode were determined to be 123, 92, 80, 64, and 57 F g^{-1}at scan rates of 1, 5, 10, 30, and 50 mV s^{-1}, respectively. The area enclosed by the cyclic voltammetry (CV) curves is observed to be directly proportional to their specific capacitance. The sharp decrease in specific capacitance at higher scan rates is due to limited ion diffusion and charge transfer kinetics, which restricts the ability to fully utilize its surface area for charge storage, whereas the specific capacitance is higher due to the availability of sufficient time for ion diffusion into the electrode, allowing greater charge accumulation. The anodic and cathodic peak currents are observed to be increasing linearly with the square root of the scan rate, indicating that the redox reaction mechanism mainly belongs to diffusion-controlled and partly capacitive-controlled.

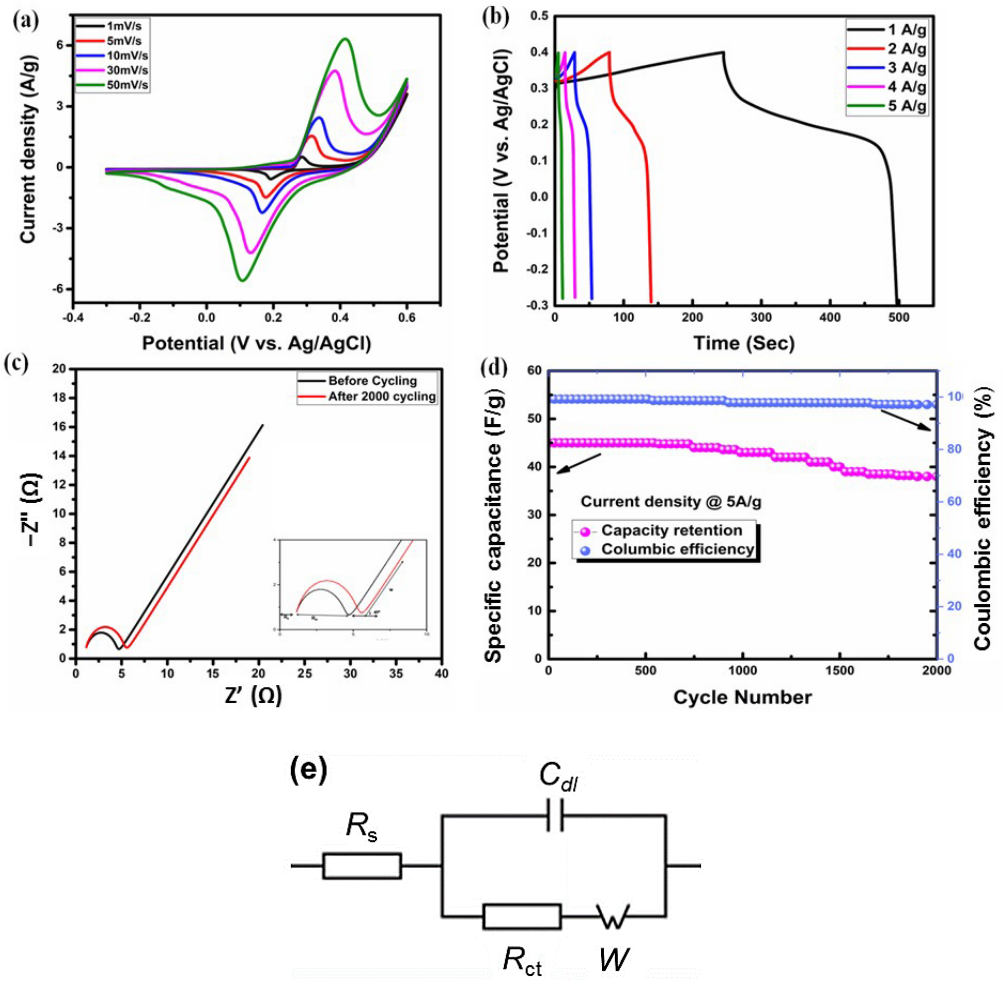


Figure 5. Electrochemical characteristics of the LTO@24 nanoflakes. (**a**) Cyclic voltammetry curves recorded at different scan rates. (**b**) Galvanostatic charge–discharge curves carried out at different current densities of 1–5 A g^{-1} in the potential range from −0.3 to 0.4 V vs. Ag/AgCl. (**c**) Nyquist plots before and after long-term cycling. Inset shows the equivalent circuit model. (**d**) Cycling stability performed at a current density of 5 A g^{-1}. (**e**) Equivalent circuit model used for the EIS fitting.

The GCD measurements were conducted under identical experimental circumstances for the LTO@24 nanoflake electrodes from −0.3 to 0.4 V vs. Ag/AgCl at various current densities ranging from 1 to 5 A g^{-1}, and the findings are presented in Figure 5b. The non-linear behavior of the plots results from fast faradic redox reactions in the LTO@24

electrodes. The specific capacitance C_s can be determined using the following Equation (7) [46,47]:

$$C_s = \frac{I\Delta t}{m\Delta V}, \quad (7)$$

where I is the discharge current, m is the mass of the active material, ΔV is the potential window, and Δt is the discharge time. The estimated specific capacities of LTO@12 and LTO@18 (from the GCD plots shown in Figures S1 and S2) are 67.0 and 97.8 F g^{-1} at 1 A g^{-1}. According to the data shown in Figure 5, the determined specific capacities of the LTO@24 nanoflakes electrode are 357, 128, 107, 85, and 45 F g^{-1}at current densities of 1, 2, 3, 4, and 5 A g^{-1}, respectively. The non-linear dependent-current responses with good symmetry at a given current density in GCD behavior indicate the Faradaic property of the electrode material. The GCD plateau demonstrates various regions: a large initial voltage drop, because of the internal resistance, a time-dependent linear deviation potential corresponding to double layer capacitance, and a marginal slope variation related to the time variation of charge transfer reaction. The voltage plateaus observed from GCD confirm the electrochemical behavior, which underwent an intercalation/deintercalation battery-type mechanism, represent a longer discharge time and high specific capacitance at lower current densities. It is evident that specific capacitance decreases as current density escalates. The observed decrease in capacitance can be ascribed to the restricted duration for electrolyte ions to infiltrate the active material when subjected to elevated current densities [48,49]. The electrochemical studies clearly demonstrate that the flake-like morphological features of the LTO@24 electrode played a key role in delivering a significant specific capacitance.

The electrochemical impedance spectroscopy (EIS) measurements were conducted prior to and after 2000 cycles, across a frequency spectrum of 1 Hz to 100 kHz, to assess electron transfer characteristics. The Nyquist plots illustrated in Figure 5c demonstrate a semicircular arc alongside and a linear segment in the low-frequency range, which indicates capacitive behavior and a rapid ion diffusion mechanism within the electrode. The solution resistance (R_s) and charge transfer resistance (R_{ct}) were estimated from the intercept and from the diameter of the semicircle, respectively. The analogous electrical circuit is depicted in Figure 5e. The results of the EIS fitting are listed in Table S1. The R_s values are recorded at 0.7 and 0.8 Ω prior to and following cycling, whereas the R_{ct} values show an increase from 2.18 to 4.8 Ω. The analysis demonstrates that the distinctive structure of $Li_4Ti_5O_{12}$ nanoflakes has the potential to enhance the faradaic active sites.

Figure 5d illustrates the long-cycle performance and Coulombic efficiency of the LTO@24. The cyclic stability holds significant importance for supercapacitor applications; therefore, an extensive examination of long-term cycling performance was conducted at a current density of 5 A g^{-1}. Additionally, the Coulombic efficiency (η) value was derived from the subsequent Equation (8) [50]:

$$\eta = \frac{t_d}{t_c} \times 100, \quad (8)$$

In this context, t_d and t_c denote the times associated with discharge and charge, respectively. The η values remain remarkably stable at approximately 98.5% for the entire 2000 cycle duration, signifying the exceptional electrochemical reversibility.

2.2. Vanadium-Doped $Li_4Ti_5O_{12}$ (V-LTO@24)

The vanadium-doped $Li_4Ti_5O_{12}$ (V-LTO@24) nanopowder was prepared under similar conditions as mentioned in Section 3.3 at low concentration (0.02 mol.%), and the microstructural and electrochemical properties.

2.2.1. Structural Studies

Figure 6a presents the X-ray diffraction spectra of V-LTO@24 ($Li_4Ti_{5-x}V_xO_{12}$; x = 0.02 mol.%) compared with pure LTO@24. No undesired impurities or new phases were observed at a lower concentration of vanadium dopant (x = 0.02), thereby affirming the successful incorporation of the vanadium ion into the lattice of $Li_4Ti_5O_{12}$ without the emergence of any additional phases, confirming the pure cubic spinel phase. Moreover, upon magnifying the peak location of the (111) plane, as seen in Figure 6b, the diffraction peak of the V-LTO@24 nanoflakes exhibits a minor shift towards a higher angle, suggesting that the doping of V has infiltrated the lattice structure of LTO nanoflakes.

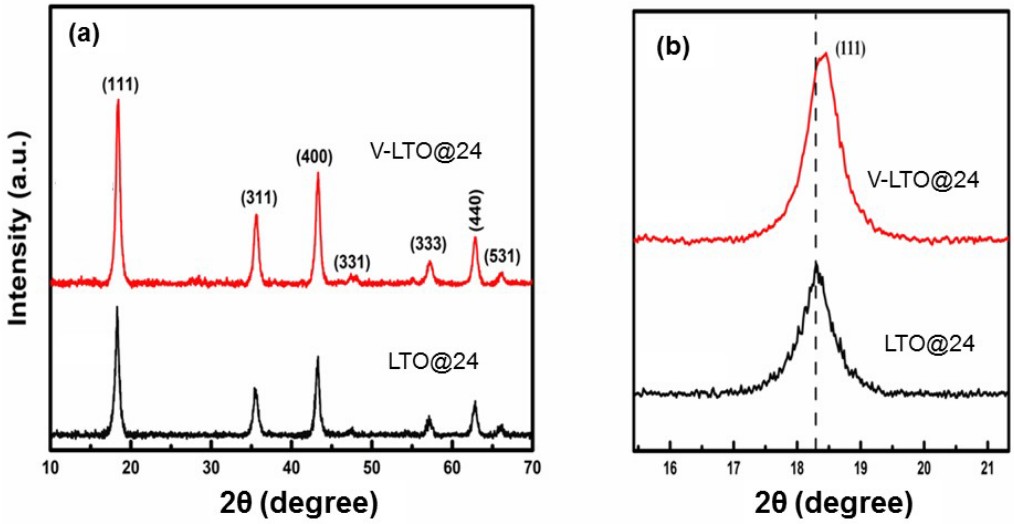


Figure 6. (**a**) XRD pattern of LTO@24 and V-LTO@24 and (**b**) expanded XRD spectrum in the vicinity of the (111) reflection.

The estimated crystallographic parameters of LTO@24 and V-LTO@24 are listed in Table 1. The results show that the lattice parameter of V-LTO@24 (a = 8.340 Å) is lower compared to that of LTO@24. This reduction suggests that V doping has induced a lattice shrinkage in the material. Such a phenomenon can be attributed to the substitution of Ti^{4+} ions (r_i = 0.605 Å) by smaller V^{5+} ions (r_i = 0.54 Å) within the spinel lattice structure of $Li_4Ti_5O_{12}$. The relatively close ionic radii facilitate the incorporation of V^{5+} into the Ti^{4+} sites with minimal distortion to the overall crystal framework. The replacement of Ti^{4+} with the smaller V^{5+} ions leads to a slight contraction of the lattice. However, the doping has significantly influenced the electrical conductivity of the host material. The measured electrical conductivity of V-LTO@24 is 3.4 × 10 $^{-4}$ S cm^{-1}, which is observed to be one order less than that of pure LTO@24 (8.2 × 10^{-6} S cm^{-1}). Such structural and electrical modifications can directly impact the electrochemical properties, potentially enhancing the material's performance in supercapacitor applications, as supported by the previous literature [28,29].

2.2.2. Surface Morphology

The surface morphological features of V-LTO@24 are shown in Figure 7. The nanoflakes evidently aggregate to create a three-dimensional nanoflower-like structure. Nonetheless, upon vanadium introduction into LTO@24, an effect of doping was noted on the surface morphology. The addition of vanadium resulted in a tighter packing of nanoflakes and the emergence of micro-network-like structures from the recrystallisation of initially formed nanoflakes. The vertically orientated arrays cross and interpenetrate, porous network-like

heterostructures offer significantly elevated active surface sites, and is advantageous for enhancing the electrochemical reactions.

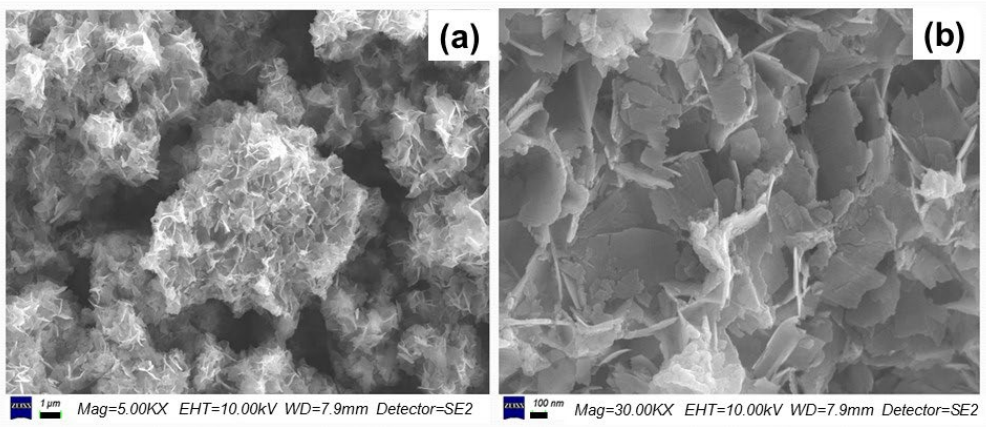


Figure 7. FESEM images for V-LTO@24 nanoflakes at different magnifications: (**a**) 1 µm scale, (**b**) 100 nm scale.

2.2.3. Electrochemical Analysis of V-LTO@24

Figure 8 presents the comprehensive electrochemical performance of V-LTO@24 electrodes. Figure 8a illustrates the CV curves of V-LTO@24 at scan rates varying from 1.0 to 50 mV s^{-1} within a potential range of −0.3 to 0.6 V vs. Ag/AgCl. The CV plots reveal a distinct difference between pure LTO@24 and V-LTO@24, highlighting the influence of vanadium doping on electrochemical properties. All the cyclic voltammetry curves display a pair of broad redox peaks with subsidized intensity and enhanced polarization value. Moreover, the V-LTO@24 exhibited more current density due to the negative impact on the redox lithiation process, which may be due to the substitution of V^{+5} in the less electroactive Ti^{+4} centers that donate the electrons to the conduction band. This leads to the enhancement of the capacitive-controlled transport mechanism. Notably, V-LTO@24 exhibited a substantially larger enclosed integral area as compared to LTO@24, indicating the greater ability to store and release charges during the electrochemical cycling, reflecting enhanced electrochemical activity. The specific capacitance (SC) values of V-LTO@24 nanostructures were found to be 413, 188, 135, 83, and 66 F g^{-1}at scan rates of 1, 5, 10, 30, and 50 mV s^{-1}, respectively. With an increase in scan rate, the region beneath the redox peaks expands, and the anodic peaks show a shift towards more positive potentials, whilst the cathodic peaks shift towards negative potentials, indicating an improvement in current responsiveness. As the scan rate increased, a gradual decrease in specific capacitance was observed.

The capacitive performance of the synthesized V-LTO@24 electrodes was thoroughly assessed by recording galvanostatic charge–discharge (GCD) data and is shown in Figure 8b. An in-depth examination of these curves demonstrated the outstanding capacitive properties of the V-LTO@24 electrodes. The estimated specific capacitances were found to be 442, 285, 171, 142, and 77 F g^{-1} at current densities of 1, 2, 3, 4, and 5 A g^{-1}, respectively. The results demonstrate the remarkable rate capability and strong electrochemical performance of the V-LTO@24 electrodes across a broad spectrum of current densities. Additionally, all GCD curves demonstrate a clear potential plateau and remarkable symmetry, affirming the high Coulombic efficiency and exceptional reversibility of the faradaic redox reactions involved.

The electrical properties of the V-LTO@24 electrode were further investigated through EIS measurements over a frequency range from 1 Hz to 100 kHz. This analysis provides critical insights into the electrode's ability to efficiently facilitate charge transfer and maintain stable performance across different frequencies. Figure 8c shows the Nyquist plot

with the equivalent circuit for the 1st and 2000th cycle. Results of the EIS fitting using the equivalent circuit model in Figure 5e (including R_s, R_{ct}, C_{dl}, and W elements) are listed in Table S2. The solution resistance (R_s) and charge transfer resistance (R_{ct}) values were found to increase from 0.38 to 0.5 Ω and from 0.6 to 0.9 Ω, respectively, and hence the decrease in specific capacitance with the number of cycles.

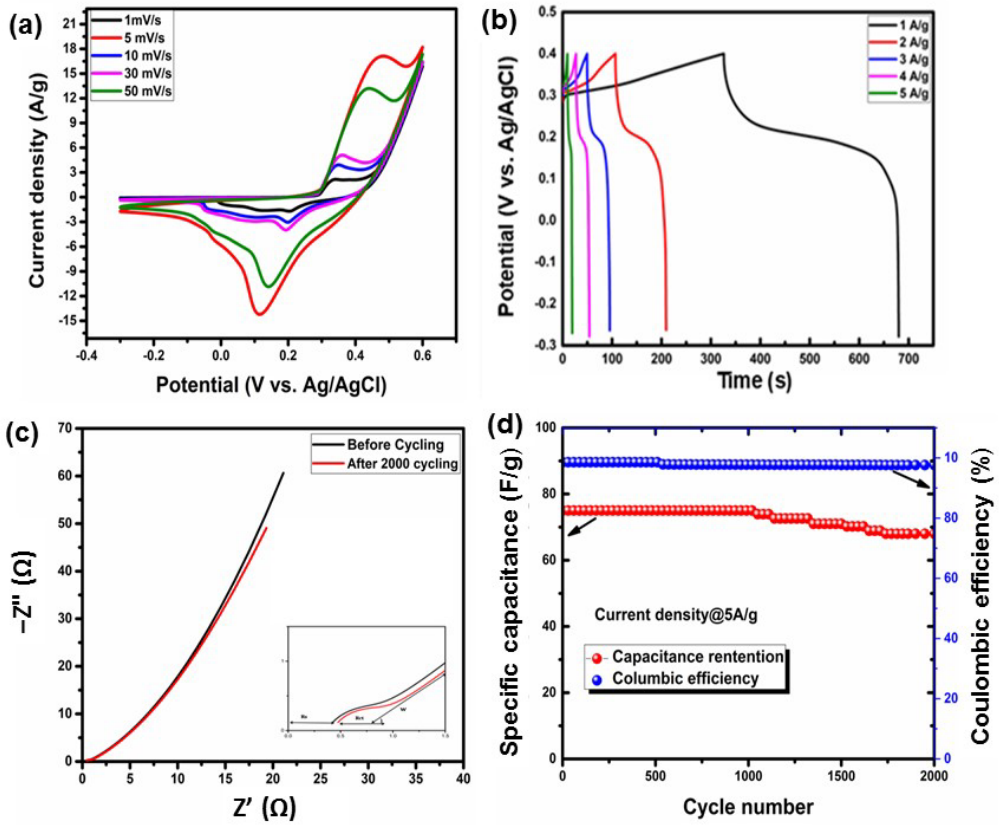


Figure 8. Electrochemical characteristics of the V-LTO@24 nanoflake electrode. (**a**) CV curves at different scan rates from 1 to 50 mV s^{-1}. (**b**) GCD profiles at different current densities. (**c**) Nyquist plots of before (black after (red curve) long-term cycling. (**d**) Cycle stability and Coulombic efficiency at current curve and density of 5 A g^{-1} over 2000 cycles.

The cycle performance of the V-LTO@24 electrode evaluated using GCD profiles is shown in Figure 8d. The results revealed that 90% of the initial capacitance was retained after 2000 cycles at a current density of 5 A g^{-1}, with a remarkable Coulombic efficiency of 99.8%. This indicates the excellent cyclic stability of the V-LTO@24 electrode. The superior electrochemical behavior of the V-LTO@24 electrode, compared to pure LTO nanoflakes, can be attributed to the aggregation of vanadium-doped LTO into a micro-network structure. The vanadium doping, along with the unique structure, not only improves the overall conductivity but also enhances the mechanical stability of the electrode during long-term cycling. The vanadium doping enhances the electrochemical reactivity, facilitates better ion diffusion, and minimizes structural degradation, which ultimately leads to better cycle stability and performance compared to pure LTO nanoflakes.

2.3. Charge Storage Mechanism in LTO-Based Electrodes

The variation of specific capacitance of the LTO@24 and V-LTO@24 electrodes collected at different scanning rates is shown in Figure 9. The decay of specific capacitance C_s is assigned to the presence of inner active sites that cannot completely sustain redox transitions at higher scanning rates [51].

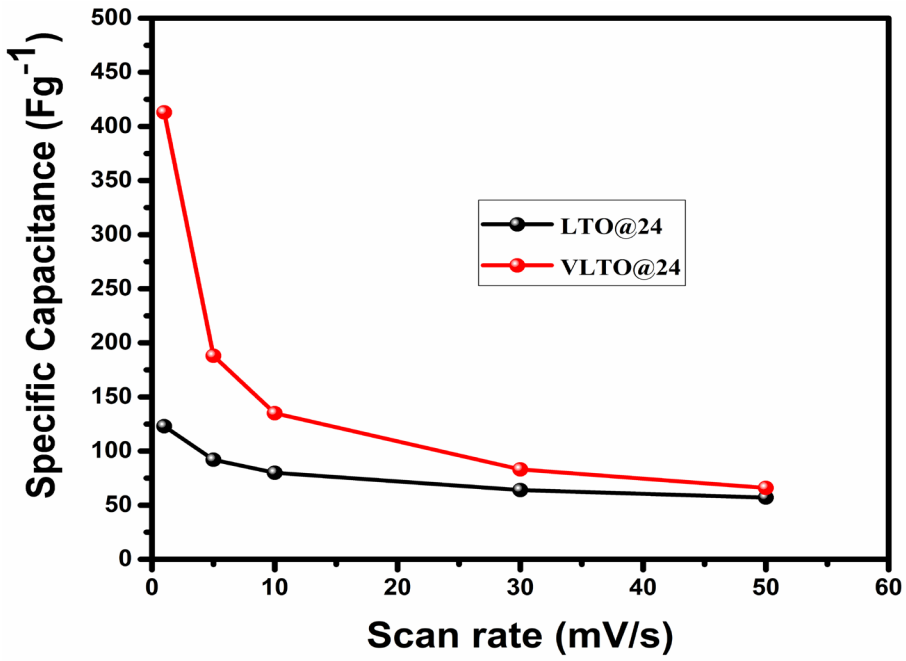


Figure 9. Specific capacitance (C_s) calculated from the CV measurements as a function of scan rate.

The reaction kinetics and charge storage mechanism in both hydrothermally prepared LTO@24 and V-LTO@24 electrodes were critically analyzed from cyclic voltammetry measurement data. The total contribution to capacitance arises from processes that are both diffusion-controlled and capacitive-controlled. Moreover, the kinetic reversibility of the electrode materials is clarified by the evident linear correlation between the peak current (i_p) and the scan rate (ν) in the CV curves, adhering to a power–law relationship, as described in Equations (9) and (10) [52]:

$$i_p = a\nu^b, \tag{9}$$

$$\log(i_p) = \log(a) + b\log(\nu), \tag{10}$$

where '*a*' and '*b*' parameters are modifiable. The slope *b* from the $\log(i_p)$ and $\log(\nu)$ of the plot indicates the charge storage kinetics of the ions. The value of *b* equal to 1.0 suggests the capacitive process as a dominant process, whereas the value of *b* equal to 0.5 suggests the diffusion control process as a dominating process. The estimated "*b*" values from the anodic peaks of the LTO@24 and V-LTO@24 electrodes are found to be 0.53 and 0.56, respectively (Figure 10a,c), indicating that the charge storage process is primarily governed by a diffusion-controlled battery-type behavior. The relative contributions of diffusion and surface capacitive processes to the total capacitance were examined via Cottrell's equation [53]:

$$i_p(\nu) = k_1\nu + k_2\nu^{1/2}, \tag{11}$$

where k_1 and k_2 are constants for specific sweep rates, $i_p(\nu)$ denotes the peak current at a given potential value, and $k_1\nu$ and $k_2\nu^{1/2}$ are terms which stand for the capacitance-controlled and diffusion-controlled processes, respectively. The above Equation (11) can be expressed as

$$i_p(\nu)\,\nu^{-1/2} = k_1\,\nu^{1/2} + k_2. \tag{12}$$

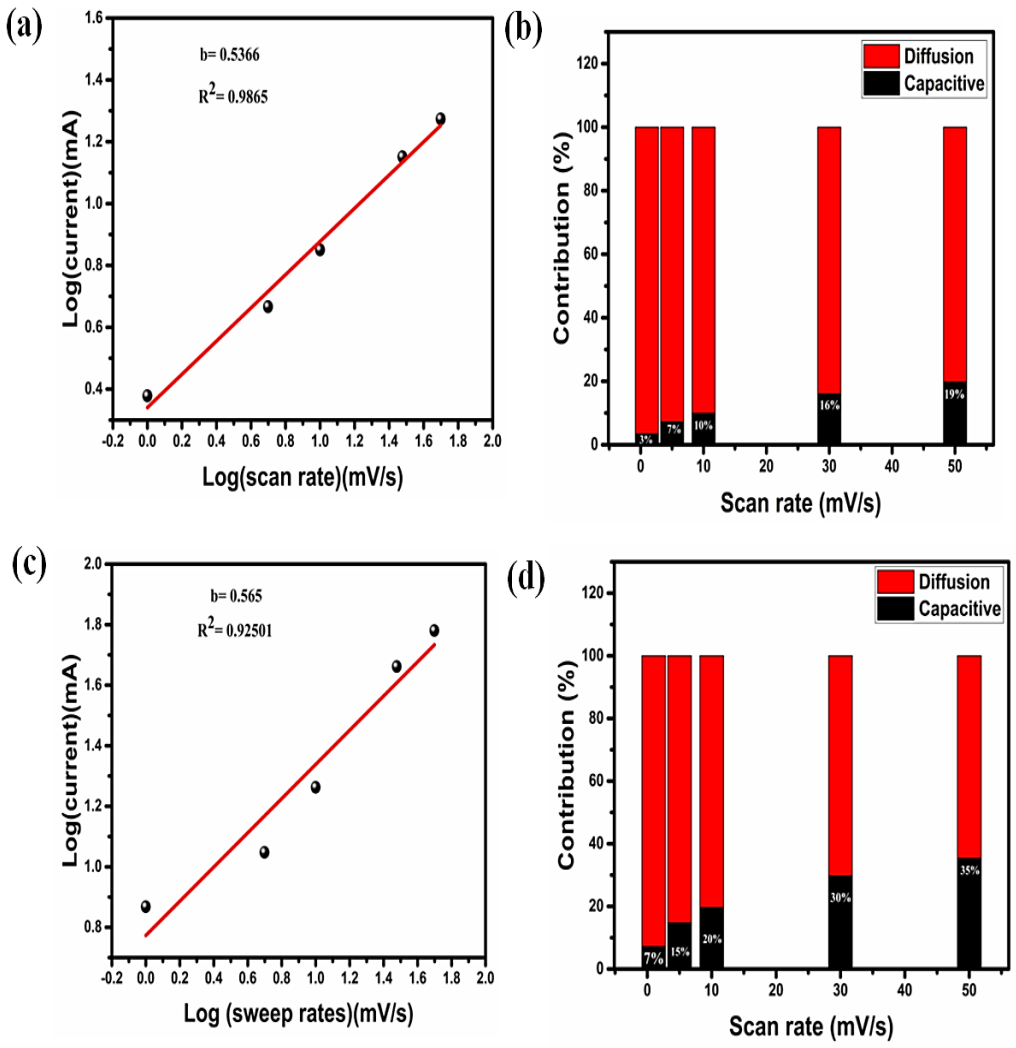


Figure 10. (**a**,**b**) Plots of log(i_p) vs. log(ν)of LTO@24 electrode at different scan rates. (**c**,**d**) Plots of log(i_p) vs. log(ν) V-LTO@24 electrode at different scan rates.

By only graphing the correlation between i_p and ν, we may ascertain the slope k_1. By determining the k_1 value at varying voltages across different scan rates [54–56], the relative contributions of the battery-type (diffusion-controlled) and capacitive-type (surface-controlled) behaviors for LTO@24 and V-LTO@24 electrodes are illustrated in Figure 10b,d. The LTO@24 and V-LTO@24 electrodes clearly demonstrate a more significant level of diffusion-controlled charge storage at all scan rates. Additionally, it has been noted that the ratio of capacitive participation across all electrodes progressively rises from lower to higher scan speeds, which can be explained by the restricted time for ions to diffuse into the internal structure of the electroactive materials.

Detailed in-depth studies of electrochemical behavior and fundamental mechanisms of the V-LTO@24 electrode uncovered several critical factors that showed enhanced supercapacitive performance, especially regarding ion transport, electron transfer processes, and microstructure. The distinctive morphology of the V-LTO@24 structure, featuring aggregated nanoflakes in a micro-network-like arrangement, is characterized by a large surface area that enhances ion transport efficiency. This configuration facilitates greater ion adsorption and desorption throughout electrochemical reactions and hence increased charge (or energy) storage within the electrode, thereby improving the specific capacitance. In addition, the successful substitution of Ti^{+4} with V^{+5} in LTO not only improved the electrical conductivity but also improved the surface charge storage kinetics of the capacitive

process at all scan rates relative to the pure LTO electrode, which favored enhanced specific capacitance and cycle stability for V-LTO@24. Furthermore, the specific capacitance and cycling stability of the LTO@24 and V-LTO@24 materials were compared with those of previously reported LTO-based electrodes, as presented in Table 2. The results demonstrate its superior electrochemical performance in a three-electrode system compared to the earlier LTO-based electrodes.

Table 2. Comparison of the electrochemical performance of hydrothermally prepared LTO@24 and V-LTO@24 electrodes with other LTO-based electrodes recently reported in the literature.

Sample	Capacitance	Retention Over Cycling	Ref.
V-doped LTO	179 mAh g^{-1} @ 1C	95% (300)	[29]
Granule-LTO powders	63 F g^{-1} @ 0.5 A g^{-1}	92.8% (7000) @ 3 A g^{-1}	[32]
SSR synthesized nano-LTO	265 F g^{-1} @ 0.5 A g^{-1}	81% (5000) @ 0.5 A g^{-1}	[35]
R-TiO_2 decorated LTO	143 mAh g^{-1} @30C	92.3% (3000)	[57]
3D chestnut shell-like LTO	653 F g^{-1} @ 1 A g^{-1}	88.5% (4000)	[36]
C-modified LTO	83 F g^{-1} @ 2C	84% (9000) @0.98 A g^{-1}	[58]
LTO nanowire	125 F g^{-1} @ 0.55 mA cm^{-2}	95% (400) @ 0.4 mA cm^{-2}	[59]
LTO–TiO_2 nanoparticles	174 mAh g^{-1} @ 2 A g^{-1}	85% (3000) @ 2 A g^{-1}	[60]
Hydrothermal LTO@24	357 F g^{-1} @ 1 A g^{-1}	98.5% (2000) @ 5 A g^{-1}	this work
Hydrothermal V-LTO@24	442 F g^{-1} @ 1 A g^{-1}	99.8% (2000) @ 5 A g^{-1}	this work

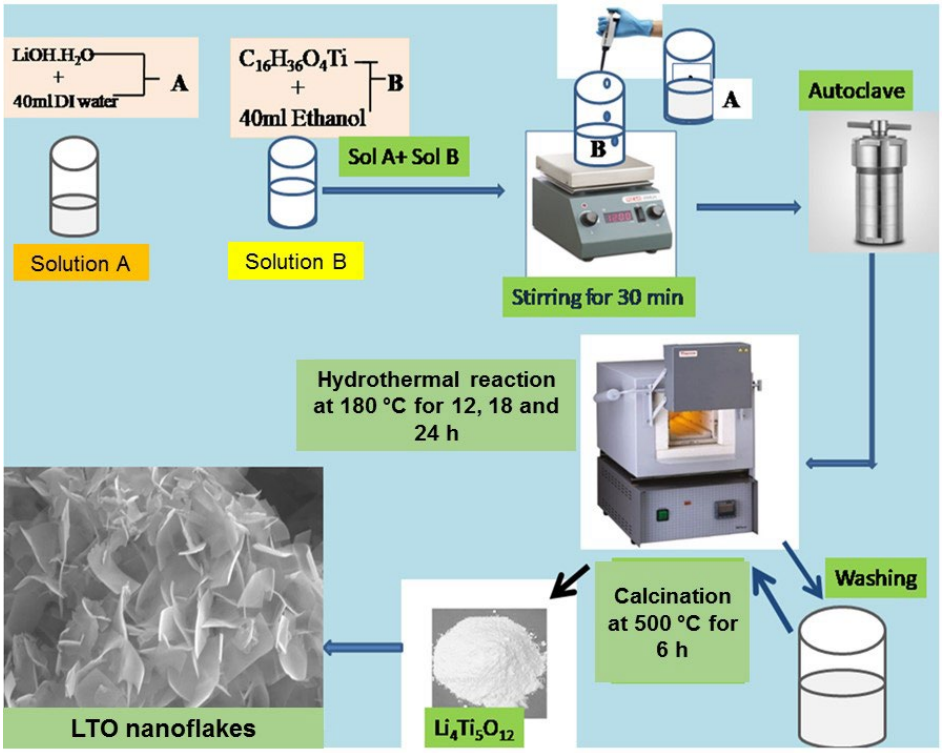
3. Materials and Methods

3.1. Materials

The chemicals used during synthesis were lithium hydroxide monohydrate (LIOH.H_2O USA), titanium(IV) butoxide ($C_{16}H_{36}O_4Ti$, ≥97% Sigma-Aldrich, St. Louis, MO, USA), ammonium metavanadate (NH_4VO_3, 99%, SDFCL), ethanol (C_2H_6O), and DI water. No additional purification procedures were implemented; all compounds were utilized entirely as received.

3.2. Preparation of $Li_4Ti_5O_{12}$ Nanomaterial

Nanostructured $Li_4Ti_5O_{12}$ samples were synthesized utilizing the hydrothermal technique (see Scheme 1). In a typical synthesis method, 4.2 mM of lithium hydroxide monohydrate ($LiOH{\cdot}H_2O$) is dissolved in 40 mL of deionized water to make solution 1, while 5 mM of titanium(IV) butoxide is dissolved in 40 mL of ethanol to create solution 2. Both solutions are stirred continuously for 30 min separately. Subsequently, solution 1 is added dropwise to solution 2 while under magnetic stirring. The homogenous solution is poured into a 100 mL autoclave. The temperature of the autoclave was maintained at 180 °C. The samples were prepared at various reaction durations (τ = 12, 18, and 24 h). The acquired material was purified and washed four times with distilled water and ethanol to ensure the solution was free of impurities. The resultant precipitate was dried at 80 °C for 5 h. Further, the final products were calcinated at 500 °C for 6 h, at a rate of 3 °C per minute, to yield $Li_4Ti_5O_{12}$nanopowders (hereinafter referred to as LTO@τ).



Scheme 1. Schematic representation of the LTO synthesis via the hydrothermal method.

3.3. Preparation of V-LTO@24 ($Li_4Ti_{5-x}V_xO_{12}$)

A similar methodology has been adopted for the preparation of vanadium-doped $Li_4Ti_5O_{12}$ nanomaterial. This involved the addition of stoichiometric amounts of ammonium meta vanadate at a concentration of 0.02% mol L^{-1}, while maintaining a hydrothermal reaction time of 24 h. The products were subjected to calcination in a muffle furnace at 500°C for a duration of 6 h to obtain the final products, designated as V-LTO@24.

3.4. Material Characterizations

The structure of the synthesized $Li_4Ti_5O_{12}$ was studied using an X-ray diffractometer (XRD, MiniFlex II, Rigaku, Tokyo, Japan) with CuKα radiation (λ = 1.540598 Å). The microstructure and surface morphology of all synthesized $Li_4Ti_5O_{12}$ powder were analyzed employing a field emission scanning electron microscope (FESEM, Merlin Compact, Carl Zeiss, Jena, Germany) and a high-resolution transmission electron microscope (TEM, Tecnai G2 F30, FEI Company, Hillsboro, OR, USA). The elemental composition data were explored using X-Ray photoelectron spectroscopy (XPS, AXIS–NOVA, Kratos). The evaluation of the electrochemical properties of the synthesized materials was performed via cyclic voltammetry (CV), galvanostatic charge and discharge (GCD), and electrochemical impedance spectroscopy (EIS) utilizing an electrochemical workstation CHI 608C (Instrument Inc., San Diego, CA, USA). EIS data were collected over a frequency range of 1 Hz–100 kHz.

3.5. $Li_4Ti_5O_{12}$ Electrode Preparation

Electrochemical evaluations were piloted at room temperature using a three-electrode setup, with Ag/AgCl as the reference electrode, and platinum as the counter electrode. Ni foam, which underwent cleaning with 6 mol L^{-1} HCl, deionized water, and 100% ethanol for 20 min each under ultrasonication to eliminate the surface layer, followed by drying at 80 °C for 10 h and was utilized as the base for the preparation of the working electrode. Subsequently, the composite comprising active material LTO@24 (80%), activated carbon black (10%), and PVDF binder (10%) was suspended in 0.5 mL of NMP solution. Activated

material slurry is applied to Ni foam (area: 0.7 × 1 cm^2) using a drop-casting technique and then dried at 80 °C for 8 h. A 1 mol L^{-1} KOH solution served as the electrolyte for all experiments.

4. Conclusions

$Li_4Ti_5O_{12}$ nanoflakes were synthesized at varying reaction durations employing a simple, inexpensive hydrothermal process. The XRD spectra validate the pure phase of $Li_4Ti_5O_{12}$ nanocomposite when synthesized at a 24 h hydrothermal reaction time. The results from SEM and TEM indicate that the LTO@24 exhibits a morphology characterized by nanoflakes with a uniform length of approximately 60 nm, a width of ~20 nm, and a relatively smooth surface. The distinct nanostructures offer an extensive surface area and minimized diffusion length, making them exceptional candidates for energy storage and conversion systems. The electrochemical investigations were conducted on the LTO@24 nanoflakes electrode using CV, GCD, and EIS experiments using a 1 mol L^{-1} KOH aqueous solution. The CV curves with marked oxidation and reduction peaks reveal the pseudocapacitive nature of the LTO electrode and demonstrate an impressive specific capacitance of 357 F g^{-1}at the current density of 1 A g^{-1}, with 84% cycle stability and 98.5% Coulombic efficiency. Moreover, the vanadium-doped LTO@24 nanoflakes synthesized under similar conditions demonstrate an excellent specific capacitance of 442 F g^{-1}at 1 A g^{-1} current density, along with 90% cycle stability and a Coulombic efficiency of 99.8%. The LTO@24 and V-LTO@24 electrodes clearly show a more significant level of diffusion-controlled charge storage at all scan rates, with significant capacitance, and are found to be suitable electrodes for high-performance supercapacitors.

Supplementary Materials: The following supporting information can be downloaded at https://www.mdpi.com/article/10.3390/inorganics13070223/s1, Figure S1: (a) CV curves of LTO@12 and (b). GCD curves of LTO@12; Figure S2: (a) CV curves of LTO@18 and (b). GCD curves of LTO@18; Table S1: ESI fitting parameters of the LTO@24 nanoflakes electrodes in three-electrode system; Table S2: ESI fitting parameters of the V-doped LTO@24 nanoflakes electrodes in three-electrode system.

Author Contributions: Conceptualization, O.M.H.; formal analysis, M.D.; investigation, M.D.; writing—original draft preparation, M.D. and O.M.H.; writing—review and editing, C.M.J. All authors have read and agreed to the published version of the manuscript.

Funding: This research received no external funding.

Institutional Review Board Statement: Not applicable.

Informed Consent Statement: Not applicable.

Data Availability Statement: All data are contained in this article.

Conflicts of Interest: The authors declare no conflicts of interest.

References

1. Peng, X.; Peng, L.; Wu, C.; Xie, Y. Two dimensional nanomaterials for flexible supercapacitors. *Chem. Soc. Rev.* **2014**, *43*, 3303–3323. [CrossRef] [PubMed]
2. Wang, H.; Casalongue, H.S.; Liang, Y.; Dai, H. $Ni(OH)_2$nanoplates grown on graphene as advanced electrochemical pseudocapacitor materials. *J. Am. Chem. Soc.* **2010**, *132*, 7472–7477. [CrossRef] [PubMed]
3. Shahid, M.; Katugampalage, T.R.; Khalid, M.; Ahmed, W.; Kaewsaneha, C.; Sreearunothai, P.; Opaprakasit, P. Microwave assisted synthesis of Mn_3O_4nanograins intercalated into reduced graphene oxide layers as cathode material for alternative clean power generation energy device. *Sci. Rep.* **2022**, *12*, 19043. [CrossRef]
4. Li, H.; Tao, Y.; Zheng, X.; Luo, J.; Kang, F.; Cheng, H.M.; Yang, Q.H. Ultra-thick graphene bulk supercapacitor electrodes for compact energy storage. *Energy Environ. Sci.* **2016**, *9*, 3135–3142. [CrossRef]

5. Lv, W.; Li, Z.; Deng, Y.; Yang, Q.H.; Kang, F. Graphene-based materials for electrochemical energy storage devices: Opportunities and challenges. *Energy Storage Mater.* **2016**, *2*, 107–138. [CrossRef]
6. Sun, J.; Luo, B.; Li, H. A review on the conventional capacitors, supercapacitors, and emerging hybrid ion capacitors: Past, present, and future. *Adv. Energy Sustain. Res.* **2022**, *3*, 2100191. [CrossRef]
7. Wang, J.; Dong, S.; Ding, B.; Wang, Y.; Hao, X.; Dou, H.; Xia, Y.; Zhang, X. Pseudocapacitive materials for electrochemical capacitors: From rational synthesis to capacitance optimization. *Natl. Sci. Rev.* **2017**, *4*, 71–90. [CrossRef]
8. Pallavolu, M.R.; Nallapureddy, J.; Nallapureddy, R.R.; Neelima, G.; Yedluri, A.K.; Mandal, T.K.; Pejjai, B.; Joo, S.W. Self-assembled and highly faceted growth of Mo and V doped ZnOnanoflowers for high-performance supercapacitors. *J. Alloys Compd.* **2021**, *886*, 161234. [CrossRef]
9. Mai, L.Q.; Yang, F.; Zhao, Y.L.; Xu, X.; Xu, L.; Luo, Y.Z. Hierarchical $MnMoO_4$/$CoMoO_4$heterostructured nanowires with enhanced supercapacitor performance. *Nat. Commun.* **2011**, *2*, 381. [CrossRef]
10. Julien, C.M.; Mauger, A. Fabrication of $Li_4Ti_5O_{12}$ (LTO) as anode material for Li-ion batteries. *Micromachines* **2024**, *15*, 310. [CrossRef]
11. Yu, L.; Chen, G.Z. Supercapatteries as high-performance electrochemical energy storage devices. *Electrochem. Energy Rev.* **2020**, *3*, 271–285. [CrossRef]
12. Raut, B.; Ahmed, M.S.; Kim, H.Y.; Rahman Khan, M.M.; Bari, G.A.R.; Islam, M.; Nam, K.W. Battery-type transition metal oxides in hybrid supercapacitors: Synthesis and applications. *Batteries* **2025**, *11*, 60. [CrossRef]
13. Devadas, A.; Baranton, S.; Napporn, T.W.; Coutanceau, C. Tailoring of RuO_2 nanoparticles by microwave assisted "Instant method" for energy storage applications. *J. Power Sources* **2011**, *196*, 4044–4053. [CrossRef]
14. Julien, C.M.; Mauger, A. Nanostructured MnO_2 as electrode materials for energy storage. *Nanomaterials* **2017**, *7*, 396. [CrossRef] [PubMed]
15. Gunasekaran, S.S.; Gopalakrishnan, A.; Subashchandrabose, R.; Badhulika, S. Phytogenic generation of NiO nanoparticles as green-electrode material for high performance asymmetric supercapacitor applications. *J. Energy Storage* **2021**, *37*, 102412. [CrossRef]
16. Haritha, B.; Deepak, M.; Hussain, O.M.; Julien, C.M. Morphological engineering of battery-type cobalt oxide electrodes for high-performance supercapacitors. *Physchem* **2025**, *5*, 11. [CrossRef]
17. Nunna, G.P.; Merum, D.; Ko, T.J.; Choi, J.; Hussain, O.M. High-performance MoO_3supercapacitor electrodes: Influence of reaction parameters on phase, microstructure, and electrochemical properties. *Int. J. Energy Res.* **2022**, *46*, 5973–5987. [CrossRef]
18. Zhang, J.C.; Liu, Z.D.; Zeng, C.H.; Luo, J.W.; Deng, Y.D.; Cui, X.Y.; Chen, Y.N. High-voltage $LiCoO_2$ cathodes for high-energy-density lithium-ion battery. *Rare Met.* **2022**, *41*, 3946–3956. [CrossRef]
19. Abou-Rjeily, J.; Bezza, I.; Laziz, N.A.; Autret-Lambert, C.; Sougrati, M.T.; Ghamouss, F. High-rate cyclability and stability of $LiMn_2O_4$ cathode materials for lithium-ion batteries from low-cost natural $\beta-MnO_2$. *Energy Storage Mater.* **2020**, *26*, 423–432. [CrossRef]
20. Borhani-Haghighi, S.; Kieschnick, M.; Motemani, Y.; Savan, A.; Rogalla, D.; Becker, H.W.; Meijer, J.; Ludwig, A. High-throughput compositional and structural evaluation of a $Li_a(Ni_xMn_yCo_z)O_r$ thin film battery materials library. *ACS Comb. Sci.* **2013**, *15*, 401–409. [CrossRef]
21. Lakshmi-Narayana, A.; Hussain, O.M.; Mauger, A.; Julien, C.M. Transport properties of nanostructured Li_2TiO_3 anode material synthesized by hydrothermal method. *Sci* **2019**, *1*, 56. [CrossRef]
22. Ohzuku, T.; Ueda, A.; Yamamoto, N. Zero-strain insertion material of $Li[Li_{1/3}Ti_{5/3}]O_4$ for rechargeable lithium cells. *J. Electrochem. Soc.* **1995**, *142*, 1431–1435. [CrossRef]
23. Ge, H.; Xie, L.; Wang, C.; Pan, R.; Huang, B.; Sun, Z.; Cao, X.; Yang, T.; Wu, G. Advanced pseudocapacitive lithium titanate towards next-generation energy storage devices. *J.Energy Chem.* **2025**, *103*, 773–792. [CrossRef]
24. Sun, C.; Ji, X.; Weng, S.; Li, R.; Huang, X.; Zhu, C.; Xiao, X.; Deng, T.; Fan, L.; Chen, L.; et al. 50C fast-charge Li-ion batteries using a graphite anode. *Adv. Mater.* **2022**, *34*, 2206020. [CrossRef] [PubMed]
25. Wang, L.; Zhang, Z.; Cheng, Y.; Zhang, Y.; Liu, W.; Su, J.; Liu, N.; Gao, Y. Revealing the phase-transition dynamics and mechanism in a spinel $Li_4Ti_5O_{12}$ anode material through in situ electron microscopy. *ACS Appl. Mater. Interfaces* **2020**, *12*, 20874–20881. [CrossRef] [PubMed]
26. Xing, L.L.; Wu, X.; Huang, K.J. High-performance supercapacitor based on three-dimensional flower-shaped $Li_4Ti_5O_{12}$-graphene hybrid and pine needles derived honeycomb carbon. *J. Colloid Interface Sci.* **2018**, *529*, 171–179. [CrossRef]
27. Lee, B.; Yoon, J.R. Preparation and characteristics of $Li_4Ti_5O_{12}$ with various dopants as anode electrode for hybrid supercapacitor. *Curr. Appl. Phys.* **2013**, *13*, 1350–1353. [CrossRef]
28. Saxena, S.; Sil, A. Role of calcination atmosphere in vanadium doped $Li_4Ti_5O_{12}$ for lithium ion battery anode material. *Mater. Res. Bull.* **2017**, *96*, 449–457. [CrossRef]
29. Khairy, M.; Bayoumy, W.A.; Qasim, K.F.; El-Shereafy, E.; Mousa, M.A. Ternary V-doped $Li_4Ti_5O_{12}$-polyaniline-graphene nanostructure with enhanced electrochemical capacitance performance. *Mater. Sci. Eng. B* **2021**, *271*, 115312. [CrossRef]

30. Batsukh, I.; Lkhagvajav, S.; Adiya, M.; Galsan, S.; Bat-Erdene, M.; Myagmarsereejid, P. Investigation of structural, optical, and electrochemical properties of niobium-doped $Li_4Ti_5O_{12}$ for high-performance aqueous capacitor electrode. *Ceram. Int.* **2023**, *49*, 26313–26321. [CrossRef]
31. Tian, Q.; Chen, P.; Zhang, Z.; Yang, L. Achievement of significantly improved lithium storage for novel clew-like $Li_4Ti_5O_{12}$ anode assembled by ultrafine nanowires. *J. Power Sources* **2017**, *350*, 49–55. [CrossRef]
32. Lee, S.H.; Kim, J.M. Improved performances of hybrid supercapacitors using granule $Li_4Ti_5O_{12}$/activated carbon composite anode. *Mater. Lett.* **2018**, *228*, 220–223. [CrossRef]
33. Putjuso, T.; Putjuso, S.; Karaphun, A.; Swatsitang, E. Influence of Li concentration on structural, morphological and electrochemical properties of anatase-TiO_2 nanoparticles. *Sci. Rep.* **2024**, *14*, 11200. [CrossRef]
34. Khanna, S.; Marathey, P.; Paneliya, S.; Chaudhari, R.; Vora, J. Fabrication of rutile–TiO_2 nanowire on shape memory alloy: A potential material for energy storage application. *Mater. Today Proc.* **2022**, *50*, 11–16. [CrossRef]
35. Chandra Sekhar, J.; Merum, D.; Hussain, O.M. Microstructural and supercapacitive performance of cubic spinel $Li_4Ti_5O_{12}$nanocomposite. *Eur. J. Mater. Sci. Eng.* **2020**, *5*, 222–233.
36. Xing, L.L.; Huang, K.J.; Cao, S.X.; Pang, H. Chestnut shell-like $Li_4Ti_5O_{12}$ hollow spheres for high-performance aqueous asymmetric supercapacitors. *Chem. Eng. J.* **2018**, *332*, 253–259. [CrossRef]
37. Sha, Y.; Zhao, B.; Ran, R.; Cai, R.; Shao, Z. Synthesis of well-crystallized $Li_4Ti_5O_{12}$nanoplates for lithium-ion batteries with outstanding rate capability and cycling stability. *J. Mater. Chem. A* **2013**, *1*, 13233–13243. [CrossRef]
38. Kalawa, O.; Sichumsaeng, T.; Kidkhunthod, P.; Chanlek, N.; Maensiri, S. Ni-doped $MnCo_2O_4$ nanoparticles as electrode material for supercapacitors. *J. Mater. Sci. Mater. Electron.* **2022**, *33*, 4869–4886. [CrossRef]
39. Aldon, L.; Kubiak, P.; Womes, M.; Jumas, J.C.; Olivier-Fourcade, J.; Tirado, J.L.; Corredor, J.I.; Pérez Vicente, C. Chemical and electrochemical Li-insertion into the $Li_4Ti_5O_{12}$ spinel. *Chem. Mater.* **2004**, *16*, 5721–5725. [CrossRef]
40. Yan, G.; Fang, H.; Zhao, H.; Li, G.; Yang, Y.; Li, L. Ball milling-assisted sol–gel route to $Li_4Ti_5O_{12}$ and its electrochemical properties. *J. Alloys Compd.* **2009**, *470*, 544–547. [CrossRef]
41. Zaghib, K.; Simoneau, M.; Armand, M.; Gauthier, M. Electrochemical study of $Li_4Ti_5O_{12}$ as negative electrode for Li-ion polymer rechargeable batteries. *J. Power Sources* **1999**, *81*, 300–305. [CrossRef]
42. Shinde, S.K.; Jalak, M.B.; Ghodake, G.S.; Maile, N.C.; Kumbhar, V.S.; Lee, D.S.; Fulari, V.J.; Kim, D.Y. Chemically synthesized nanoflakes-like $NiCo_2S_4$ electrodes for high-performance supercapacitor application. *Appl. Surface Sci.* **2019**, *466*, 822–829. [CrossRef]
43. Xia, H.; Xu, Q.; Zhang, J. Recent progress on two-dimensional nanoflake ensembles for energy storage applications. *Nano-Micro Lett.* **2018**, *10*, 66. [CrossRef] [PubMed]
44. Le, P.A.; Le, V.Q.; Tran, T.L.; Nguyen, N.T.; Phung, T.V.B.; Dinh, V.A. Two-dimensional $NH_4V_3O_8$nanoflakes as efficient energy conversion and storage materials for the hydrogen evolution reaction and supercapacitors. *ACS Omega* **2022**, *7*, 25433–25442. [CrossRef]
45. Pawar, S.M.; Kim, J.; Inamdar, A.I.; Woo, H.; Jo, Y.; Pawar, B.S.; Cho, S.; Kim, H.; Im, H. Multi-functional reactively-sputtered copper oxide electrodes for supercapacitor and electro-catalyst in direct methanol fuel cell applications. *Sci. Rep.* **2016**, *6*, 21310. [CrossRef]
46. Zhu, J.; Song, D.; Pu, T.; Li, J.; Huang, B.; Wang, W.; Zhao, C.; Xie, L.; Chen, L. Two-dimensional porous $ZnCo_2O_4$ thin sheets assembled by 3D nanoflake array with enhanced performance for aqueous asymmetric supercapacitor. *Chem. Eng. J.* **2018**, *336*, 679–689. [CrossRef]
47. Naresh, B.; Kuchi, C.; Rajasekhar, D.; Reddy, P.S. Solvothermal synthesis of $MnCo_2O_4$ microspheres for high-performance electrochemical supercapacitors. *Colloids Surf. A: Physicochem. Eng. Asp.* **2022**, *640*, 128443. [CrossRef]
48. Saraf, M.; Natarajan, K.; Mobin, S.M. Emerging robust heterostructure of MoS_2–rGO for high-performance supercapacitors. *ACS Appl. Mater. Interfaces* **2018**, *10*, 16588–16595. [CrossRef]
49. Sheokand, S.; Kumar, P.; Jabeen, S.; Samra, K.S. 3D highly porous microspherical morphology of NiO nanoparticles for supercapacitor application. *J. Solid State Electrochem.* **2023**, *27*, 727–738. [CrossRef]
50. Shaik, D.P.; Kumar, M.S.; Reddy, P.N.K.; Hussain, O.M. High electrochemical performance of spinel Mn_3O_4 over Co_3O_4nanocrystals. *J. Molecular Struct.* **2021**, *1241*, 130619. [CrossRef]
51. Pawar, S.M.; Inamdar, A.I.; Gurav, K.V.; Jo, Y.; Kim, H.; Kim, J.H.; Im, H. Effect of oxidant on the structural, morphological and supercapacitive properties of nickel hydroxide nanoflakes electrode films. *Mater. Lett.* **2015**, *141*, 336–339. [CrossRef]
52. Xi, Y.; Xiao, Z.; Lv, H.; Sun, H.; Zhai, S.; An, Q. Construction of CuO/Cu-nanoflowers loaded on chitosan-derived porous carbon for high energy density supercapacitors. *J. Colloid Interface Sci.* **2023**, *630*, 525–534. [CrossRef]
53. Merum, D.; Nallapureddy, R.R.; Pallavolu, M.R.; Mandal, T.K.; Gutturu, R.R.; Parvin, N.; Banerjee, A.N.; Joo, S.W. Pseudocapacitive performance of freestanding $Ni_3V_2O_8$nanosheets for high energy and power density asymmetric supercapacitors. *ACS Appl. Energy Mater.* **2022**, *5*, 5561–5578. [CrossRef]

54. Pallavolu, M.R.; Banerjee, A.N.; Joo, S.W. Battery-type behavior of Al-doped CuO nanoflakes to fabricate a high-performance hybrid supercapacitor device for superior energy storage applications. *Coatings* **2023**, *13*, 1337. [CrossRef]
55. Ajay, A.; Paravannoor, A.; Joseph, J.; Anopp, A.V.; Nair, S.V.; Balakrishnan, A. 2 D amorphous frameworks of $NiMoO_4$ for supercapacitors: Defining the role of surface and bulk controlled diffusion processes. *Appl. Surface Sci.* **2015**, *326*, 39–47. [CrossRef]
56. Hussain, M.N.; Inayat, A.; Ansir, R.; Naveed, A.; Abbas, S.M.; Haider, A.; Shah, S.M. Probing the synergy of $Ni(OH)_2$/NiO nanoparticles supported on rGO for battery-type supercapacitors. *Energy Technol.* **2024**, *12*, 2300854. [CrossRef]
57. Gao, L.; Huang, D.; Shen, Y.; Wang, M. Rutile-TiO_2decorated $Li_4Ti_5O_{12}$nanosheet arrays with 3D interconnected architecture as anodes for high performance hybrid supercapacitors. *J. Mater. Chem. A* **2015**, *3*, 23570–23576. [CrossRef]
58. Ni, J.; Yang, L.; Wang, H.; Gao, L. A high-performance hybrid supercapacitor with $Li_4Ti_5O_{12}$-C nano-composite prepared by in situ and ex situ carbon modification. *J. Solid State Electrochem.* **2012**, *16*, 2791–2796. [CrossRef]
59. Zuo, W.; Wang, C.; Li, Y.; Liu, J. Directly grown nanostructured electrodes for high volumetric energy density binder-free hybrid supercapacitors: A case study of CNTs//$Li_4Ti_5O_{12}$. *Sci. Rep.* **2015**, *5*, 7780. [CrossRef]
60. Gangaja, B.; Nair, S.V.; Santhanagopalan, D. Interface-engineered $Li_4Ti_5O_{12}$–TiO_2 dual-phase nanoparticles and CNT additive for supercapacitor-like high-power Li-ion battery applications. *Nanotechnology* **2018**, *29*, 095402. [CrossRef]

Disclaimer/Publisher's Note: The statements, opinions and data contained in all publications are solely those of the individual author(s) and contributor(s) and not of MDPI and/or the editor(s). MDPI and/or the editor(s) disclaim responsibility for any injury to people or property resulting from any ideas, methods, instructions or products referred to in the content.